



Study of Sintering Temperature Effects on the Structural and Electrical Properties of $\text{Mg}_{0.6}\text{Co}_{0.4}\text{FeCrO}_4$ Ferrites Synthesized by the Sol–Gel Method

Mongi Chebbi^{1,2} · Salaheddine Mansouri² · Sobhi Hcini² · Nejeh Hamdaoui³ · Lassaad El Mir¹

Received: 20 November 2022 / Accepted: 3 February 2023 / Published online: 16 February 2023
© The Author(s), under exclusive licence to Springer Science+Business Media, LLC, part of Springer Nature 2023

Abstract

In the present study, $\text{Mg}_{0.6}\text{Co}_{0.4}\text{FeCrO}_4$ ferrite samples were synthesized by sol–gel method at 900 °C and 1100 °C. We have studied in detail the effect of the sintering temperature on their structural, infrared, electrical and dielectric properties. The results showed that by increasing the sintering temperature, the lattice constant, the grain size, the intensities of absorption bands, the conductivity and dielectric constants of the samples increase. The X-ray diffraction results show that our samples crystallize in the cubic structure with $\text{Fd}\bar{3}\text{m}$ space group. FTIR spectra showed an absorption band corresponded to metal–oxygen stretching vibration in the tetrahedral sites. A metal–semiconductor transition was observed for the samples at a specific temperature T_{MS} . When the sintering temperature increases, the value of the electrical conductivity increases, however the transition temperature (T_{MS}) between metal and semi-conductor behaviors remains unchanged. Dielectric constants rapidly decrease as frequency rises. This phenomenon has been explained using the Maxwell–Wagner theory of interfacial polarization. The electrical modulus and impedance investigation demonstrate that the samples exhibit an electrical relaxation phenomenon that is not of the Debye type. The equivalent electrical circuit with $[\text{R}_g // \text{CPE}_g + \text{R}_{gb} // \text{CPE}_{gb}]$ configuration is the most appropriate model to modelize the prepared samples. The activation energies calculated from the dc conductivity, impedance, and modulus studies are quite close, indicating that the relaxation and conduction processes are caused by the same defect.

Keywords Ferrites · Sol–gel method · Metal semiconductor transition · Sintering temperature · Relaxation phenomenon

1 Introduction

Ferrites with a spinel structure have a chemical formula of $(\text{Me}_{1-\delta}^{2+}\text{Fe}_{\delta}^{3+})[(\text{Me}_{\delta}^{2+}\text{Fe}_{2-\delta}^{3+})\text{O}_4]^{2-}$, where parentheses and square brackets denote the cation sites of tetrahedral (A) and octahedral (B) coordination, respectively [1, 2]. δ represents the

degree of inversion expressed as the fraction of the (A) sites occupied by Fe^{3+} ions. Spinel ferrites is classified into three categories (normal spinel structure if $\delta = 1$; inverse spinel structure if $\delta = 0$ and mixed spinel structure if $0 < \delta < 1$).

Ferrites are the subject of intensive scientific investigation in order to improve their functionality for technological applications [3]. Ferrites have intriguing physical features, such as their structural, electric, dielectric, magnetic, and optical properties, making them valuable materials for technology [4]. Nowadays with the development of technology the ferrites are also promising candidates for various technological applications, such as microwave absorption, ferrofluids, humidity sensor and photo detectors, as well as high density storage devices [5], biosensing, MRI technology with variable magnetic characteristics, electronic devices, and medication delivery [6], biomedical applications like drug delivery system, dye-sensitized solar cells, high frequency transformers, biomedical applications like drug delivery system and so on [7], magnetic refrigeration

✉ Salaheddine Mansouri
mansourislah@gmail.com

¹ Faculty of Sciences of Gabes, Laboratory of Physics of Materials and Nanomaterials Applied at Environment (LaPhyMNE), Gabes University, Erriadh Zrig City, 6072 Gabes, Tunisia

² Faculty of Sciences and Technology of Sidi-Bouزيد, University Campus Agricultural City, University of Kairouan, 9100 Sidi Bouزيد, Tunisia

³ Institut Supérieur des Technologies de l'Informatique et de la Communication, Université de Sousse, Gp1, 4011 Hammam Sousse, Tunisia

systems, gas sensing, catalytic application and so on [8]. However, the electrical characteristics of spinel ferrites must be improved in order to enhance their electronic applications. It is crucial to examine their dielectric behavior at various frequencies in this situation.

Spinel ferrites have been prepared using several synthesis methods among them we can cite the electrochemical [9], plasma synthesis [10], co-precipitation [11], hydrothermal [12], sol–gel [13], the reverse micelle [14], and the citrate precursor [15] methods. According to a review of the literature, the preparation technique, concentration, chemical composition, porosity, type of substituted element, sintering temperatures, grain size, microstructure, heat treatment, difference in ionic radii and the distribution of metallic ions among crystallographic crystal lattice sites are the main factors that affect the dielectric properties of ferrites [16, 17].

Cobalt ferrite (CoFe_2O_4), one of the spinel ferrites, has received a lot of attention recently because to its important electrical characteristics, including low eddy current, high dielectric constant, low dielectric losses, and high resistivity [18] and magnetic properties like the highest values of magneto-crystalline anisotropy and magnetostriction [19], high coercivity, moderate saturation magnetization [20]. These characteristics make cobalt ferrite a viable substance for use in the creation of computer memory systems, solar cells, microwave, drug delivery, actuators, Li batteries and super capacitors [21, 22]. Magnesium ferrite (MgFe_2O_4) is a promising candidate for a variety of applications due to its low dielectric losses, low magnetic and high electrical resistivity. These applications include usage in sensors and electronic device, noise filters, fabrication of radio frequency coils [23], catalyst, humidity sensor [24], microwave absorption, semiconductors, magnetic applications including transformers and gas sensor [25].

The studies revealed that the magnetic characteristics of the ($\text{MgFe}_{2-x}\text{Cr}_x\text{O}_4$) ferrites are significantly altered when iron is replaced with chromium [26]. Mg ferrite with Cr substitution ($\text{MgFe}_{2-x}\text{Cr}_x\text{O}_4$) is appropriate for the long wave region of the high frequency spectrum because to extraordinarily low dielectric losses [27].

The study of the chromium substituted cobalt ferrites ($\text{CoFe}_{2-x}\text{Cr}_x\text{O}_4$) show only with increase of Cr^{3+} content the coercivity has decreased [28], magnetostriction coefficient values are increased [29], the magnetization has decreased, and the compounds are being converted into soft magnetic materials [30]. The $\text{CoFe}_{2-x}\text{Cr}_x\text{O}_4$ ferrites are used in biotechnological application, sensors, high density magnetic information storage, recording tapes, high quality digital printing, switching devices, microwave devices, transducers, actuators [18].

In this regard the study of the properties of Cr-substituted $\text{MgCoFe}_2\text{O}_4$ with formula ($\text{Mg}_{0.6}\text{Co}_{0.4}\text{FeCrO}_4$) is interesting. In present work, the investigation is concerned with

the preparation of the ($\text{Mg}_{0.6}\text{Co}_{0.4}\text{FeCrO}_4$) ferrite and the effect of sintering temperatures (900 and 1100 °C) on the structural characteristics, on the IR bands as well as the dielectric properties of samples. The sol–gel technique is used to create the sample. It is one of the most exploited methods for the preparation of ferrite samples. It is a simple and affordable chemical process which is mainly used to generate ultrafine powder with limited size distribution in a fairly short time and at low temperature. It also improves the product's purity, stoichiometry and homogeneity [31, 32]. At room temperature, the structural characterization was carried out and the impedance spectroscopy method was utilized to ascertain the dielectric properties as a function of frequency and temperature.

2 Experimental Methods

2.1 Preparation

The sol–gel process was used to prepare the $\text{Mg}_{0.6}\text{Co}_{0.4}\text{FeCrO}_4$ ferrites using stoichiometric quantities of $\text{Mg}(\text{NO}_3)_2 \cdot 6\text{H}_2\text{O}$, $\text{Co}(\text{NO}_3)_2 \cdot 6\text{H}_2\text{O}$, $\text{Fe}(\text{NO}_3)_3 \cdot 9\text{H}_2\text{O}$, $\text{Cr}(\text{NO}_3)_3 \cdot 9\text{H}_2\text{O}$ precursors and citric acid of formula $\text{C}_6\text{H}_8\text{O}_7\text{H}_2\text{O}$. All these compounds have a purity of 99.9%. The samples whole synthesis procedure is shown in Fig. 1. The samples were synthesized by mixing stoichiometric amounts of metal nitrates in 150 ml distilled water while thermally stirring at 95 °C to create a mixed solution. After the nitrates had completely dissolved in the solution, controlled amounts of citric acid, which is employed as a complexing agent for various metal ions, were added and dissolved with stirring. Nitrates and citric acid were mixed at a 1:1 molar ratio. After that, a small amount of ammonia was added to the solution to bring the pH level down to roughly 7. Following this step, ethylene glycol (which has been employed as an agent for polymerization) was added and the resultant solution was heated for 4 h on a hot plate with vigorous stirring until the gel was produced. The latter was heated in oven for 12 h at 250 °C to obtain a foamy dry which is ground with a mortar. Then, the powders were ground and calcined for 24 h at 800 °C after being annealed at 600 °C for 12 h. The final step was to press the resulting $\text{Mg}_{0.6}\text{Co}_{0.4}\text{FeCrO}_4$ powders into pellets with a diameter of 10 mm and a thickness of roughly 2 mm under 100 MPa. The pellets were then split into two portions and sintered separately for 24 h at 900 °C and 1100 °C, respectively.

2.2 Characterizations

The crystal structure and phase purity of each sample was examined by X-ray diffraction (XRD) using a “PANalytical X'Pert Pro” diffractometer with $\text{CuK}\alpha$ radiation

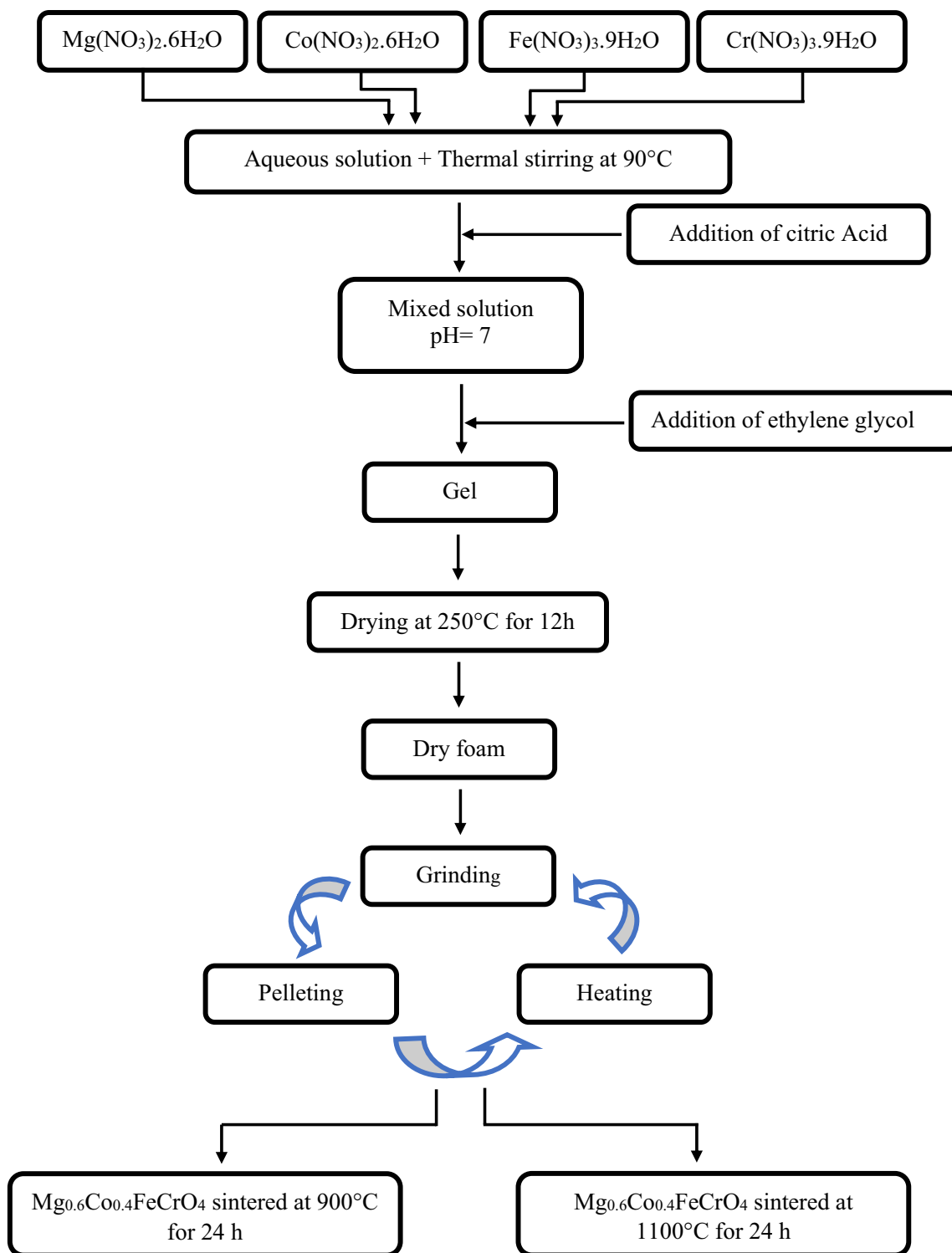


Fig. 1 Detailed schematic representation of the synthesis for $\text{Mg}_{0.6}\text{Co}_{0.4}\text{FeCrO}_4$ ferrite by the sol-gel method

($\lambda = 1.5406 \text{ \AA}$) and a nickel filter to block the $\text{K}\beta$ ray in the $20^\circ\text{--}80^\circ$ range. The FTIR spectra studies were carried out at room temperature at room temperature with a wave number range of 450 to 4000 cm^{-1} and a resolution

of 1 cm^{-1} using a Shimadzu Fourier Transform Infrared Spectrophotometer (FTIR-8400S). Electrical characterizations have been done by using an instrument called N4L-NumetriQ (model PSM1735) analyzer at different

temperatures ranging from 300 to 600 K in the 10^2 – 10^6 Hz frequency range.

3 Results and Discussions

3.1 Structural Analyses

The X-ray diffraction patterns for $\text{Mg}_{0.6}\text{Co}_{0.4}\text{FeCrO}_4$ ferrites sintered at two different temperatures (900 °C and 1100 °C) are shown in Fig. 2. It can be noticed that all of the Bragg reflections have the following designations: (220), (311), (222), (400), (422), (511), (440), (620), (533), (622) and (444) [33]. Our samples reveal a cubic crystal structure with the $\text{Fd}\bar{3}\text{m}$ space group, and there are no apparent secondary crystallographic phases of impurities. The absence of further impurity-related peaks shows that our samples are of excellent purity. The Table 1 presents all the refined structural parameters of the samples. We suggested the cation distribution $(\text{Fe}^{3+})_{\text{A}}[\text{Mg}_{0.6}^{2+}\text{Co}_{0.4}^{2+}\text{Cr}_1^{3+}]_{\text{B}}\text{O}_4^{2-}$ for the Rietveld refinement technique. The atomic positions for the cations occupying the tetrahedral site (A) are 8a (1/4, 1/4, 1/4), those for the cations occupying the octahedral site [B] are 16d (1/2, 1/2, 1/2) and those for O are 32e (x, y, z). We have shown from the XRD patterns that the intense peak (3 1 1) exhibits a little shift towards a lower diffraction angle (2θ) as the sintering temperature rises. This leads us to the conclusion that the lattice parameters increase slightly with the

sintering temperature. Moreover, we see that the width of the peak decreases and its intensity increases as the sintering temperature increases. This one is due to the thermally activated enhancement of crystalline structure. The lattice parameter and cell volume in the samples increased with increasing sintering temperature. This shows the relaxation of the lattice structure at higher sintering temperatures [34]. The samples sintered at 900 °C and 1100 °C have lower lattice constants than those of the parent compound $\text{Mg}_{0.6}\text{Co}_{0.4}\text{Fe}_2\text{O}_4$ [35]. This is due to the lower ionic radius of Cr^{3+} ($r_{\text{Cr}^{3+}} = 0.63 \text{ \AA}$) than Fe^{3+} ($r_{\text{Fe}^{3+}} = 0.67 \text{ \AA}$) [36]. The following equation was used to calculate the X-ray density [37]:

$$d_x = \frac{8M}{Na^3} \quad (1)$$

where N is the Avogadro's number, M is the sample's molecular weight, and 8 is the number of molecules in a spinel lattice unit cell. Using the most intense diffraction peak (311), the average crystallite size was calculated using XRD patterns in accordance with the Debye–Scherrer relation [38, 39]:

$$C_s = \frac{0.9\lambda}{\beta \cos\theta} \quad (2)$$

where β is the full-width at half-maximum of the (311) peak, θ is the diffraction angle and λ is the X-ray wavelength of

Fig. 2 The XRD patterns for $\text{Mg}_{0.6}\text{Co}_{0.4}\text{FeCrO}_4$ ferrites sintered at 900 °C and 1100 °C

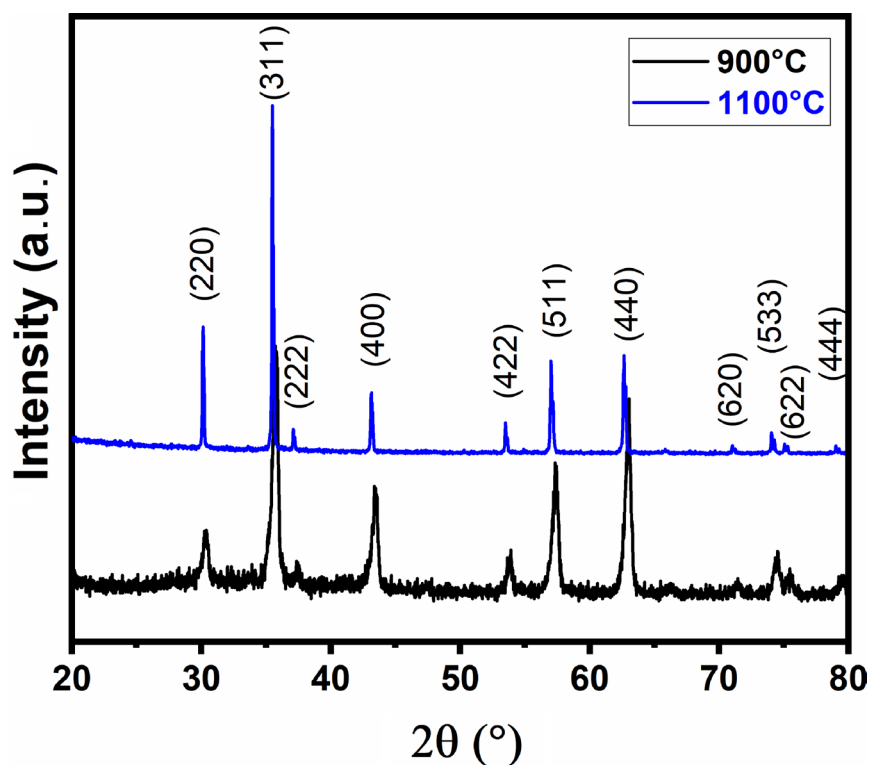


Table 1 Structural parameters determined after structural refinement according to the Rietveld method for $Mg_{0.6}Co_{0.4}FeCrO_4$ ferrites sintered at 900 °C and 1100 °

$Mg_{0.6}Co_{0.4}FeCrO_4$		900 °C	1100 °C
Space group		Fd $\bar{3}m$	
Cell parameters		a (Å)	8.3552 (1) 8.3852 (1)
Cell volume		V (Å ³)	583.27 589.569
Wyckoff positions		8a 8a	
Site symmetry		– 43 m – 43 m	
Fe	Atomic positions	x = y = z	0.125 0.125
	Occupancy factors	1 1	
	Biso (Å ²)	1.32 (0) 1.14 (2)	
	Wyckoff positions	16d 16d	
	Site symmetry	– 3 m – 3 m	
Atoms	Mg /Co/Cr	Atomic positions	x = y = z 0.5 0.5
	Occupancy factors	0.6/0.4/1 0.6/0.4/1	
	Biso (Å ²)	1.07 (0) 1.21 (2)	
	Wyckoff positions	32e 32e	
	Site symmetry	3 m 3 m	
O	Atomic positions	x = y = z	0.2625 (6) 0.2623 (6)
	Occupancy factors	4 4	
	Biso (Å ²)	1.85 (0) 1.70 (2)	
	R_A (Å)	1.961 (7) 1.957 (5)	
	R_B (Å)	2.016 (7) 2.005 (5)	
Structural Parameters	θ_{A-O-B} (°)	122.1 (3) 122.8 (2)	
	θ_{B-O-B} (°)	95.3 (3) 94.8 (2)	
	C_s (nm)	48 56	
	d_x (g cm ⁻³)	4.7831 4.732	
Structural Parameters	R_p (%)	8.45 8.34	
	R_{wp} (%)	10.3 10.9	
	R_F (%)	3.91 3.95	
	χ^2 (%)	1.19 1.62	

C. B_{iso} : isotropic thermal agitation parameter; R_A distance (Fe – O); R_B distance (Mg, Co, Cr – O); θ_{A-O-B} : angle (Fe – O – Mg, Co, Cr); θ_{B-O-B} : angle (Mg, Co, Cr – O – Mg, Co, Cr); C_s : crystallites size; d_x : X-ray density. Agreement factors of profile R_p , weighted profile R_{wp} , and structure R_F . χ^2 : the goodness of fit. The numbers in parentheses are estimated standard deviations to the last significant digit.

the Cu- k_α radiation ($\lambda = 1.5418$ Å). Figure 3 shows good agreement between the calculated and observed profiles. The results presented in Table 1 show that when the sintering temperature increases, the grain size increases. During sintering, many crystallites with the same orientation fuse and form a large grain. The increase in grain size with increasing sintering temperature is due to recrystallization of samples and increase in unit cell volume. Indeed, the tendency of crystallites to join together and constitute large grains is evidently realized in the sample sintered at 1100 °C than the one sintered at 900 °C [40].

3.2 FTIR Spectrum Analysis

Infrared spectroscopy is used to locate ions in crystals and identify functional groups in materials by analyzing vibrational modes [41, 42]. In general, the FTIR spectra of ferrites

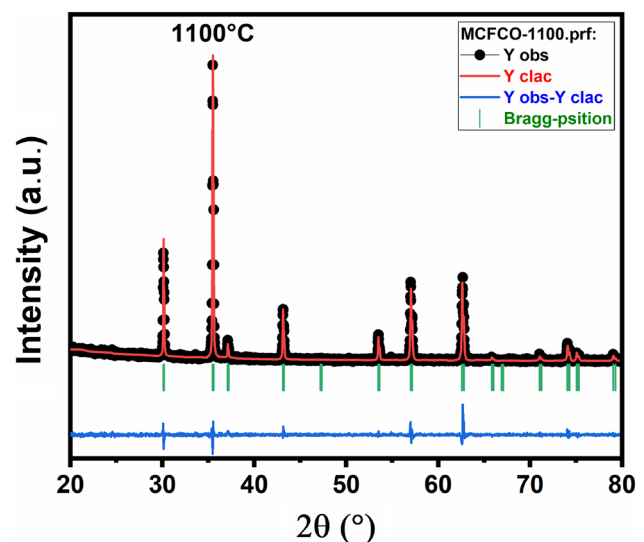


Fig. 3 Typical example for the Rietveld refinement of the XRD pattern for $Mg_{0.6}Co_{0.4}FeCrO_4$ ferrite sintered at 1100 °C

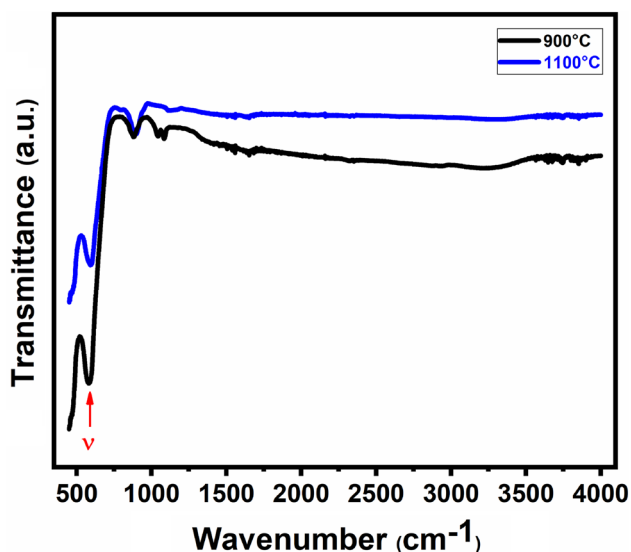


Fig. 4 FTIR spectra for $\text{Mg}_{0.6}\text{Co}_{0.4}\text{FeCrO}_4$ ferrites sintered at 900 °C and 1100 °C

include two distinct absorption peaks, which are related to oxygen bond vibrations with metal cations in tetrahedral and octahedral sites [43, 44]. Generally, the strongest and most apparent peaks are between 350 and 700 cm^{-1} . Their location and intensities depend on the type of cations present and how they are distributed among the sublattices [45]. FTIR spectrum for $\text{Mg}_{0.6}\text{Co}_{0.4}\text{FeCrO}_4$ ferrites measured in the 450 to 4000 cm^{-1} frequency range as depicted in Fig. 4. The spectra revealed the existence of two vibration bands at about 582.876 cm^{-1} for the sample sintered at 900 °C and 597.383 cm^{-1} for the one sintered at 1100 °C, which are related to the stretching vibration caused by the interactions between Metal–oxygen in the tetrahedral site [46]. As the sintering temperature rises, the values of ν_A rise. This rise is explained by a reduction in the R_A distances between the cations at the tetrahedral sites and oxygen as a result of an increase in sintering temperature [47]. When the sintering temperature is high, the value of ν_A shifts to a higher frequency due to a significant improvement in the crystallinity of the samples [48]. However, the FTIR spectra also show the presence of a peak at 883 cm^{-1} , which indicates the presence of a C–H bending vibration [49]. The clear band that appears at 1100 cm^{-1} is mainly due to the coupling bending vibrations O–H and stretching vibrations C–O [50]. The observed peak at frequency 1635 cm^{-1} is attributed to both the stretching vibration and the bending vibration of the H–O–H bond [51]. The band between 3570 and 3900 cm^{-1} is due to the stretching vibrations of the water which is absorbed by the surfaces of the samples [48]. The force constant K_T for the tetrahedral site is determined using the following equation [52]:

$$K_T = 7.62M_A\nu_A^2 \cdot 10^{-3} (\text{dyne/cm}) \quad (3)$$

where M_A represents the average molecular mass of the entity formed by the cations existing in the tetrahedral site. The determined values of the force constant K_T are grouped in Table 2. According to the results presented in this table, it can be seen that the K_T value increases as the sintering temperature increase. The increase in K_T with increasing sintering temperature is also due to the decrease in bond length R_A , which is established between the cations and the oxygen of the tetrahedral sites [53].

3.3 Electrical Conductivity

Figure 5 shows the variation of electrical conductivity (σ) with frequency at various temperatures for $\text{Mg}_{0.6}\text{Co}_{0.4}\text{FeCrO}_4$ ferrites. The following equation is used to calculate the conductivity of these samples [54]:

$$\sigma = \left(\frac{e}{s} \right) \left[\frac{Z'^2}{Z'^2 + Z''^2} \right] \quad (4)$$

where e is the thickness of the pellets and s is its area, (Z') is the real part and (Z'') the imaginary part of the complex impedance. Moreover, the following formula analyzes the phenomenon of dispersion of the conductivity [54]:

$$\sigma = \left[\frac{\sigma_s}{(1 + \tau^2\omega^2)} \right] + \left[\frac{(\sigma_\infty \tau^2\omega^2)}{(1 + \tau^2\omega^2)} \right] + A\omega^s \quad (5)$$

where σ_s and σ_∞ denote respectively the values of the conductivity at low and high frequencies, τ is the relaxation time, A is a pre-factor which is influenced by both composition and temperature, ‘ s ’ represents the frequency exponent and $\omega = 2\pi f$ represents the angular frequency. The change of exponents with the evolution of the temperature gives an idea of the possible conduction model. There is a physical significance to the value of ‘ s ’. When $s \leq 1$, the electron is abruptly hopping while also traveling in translation. While $s > 1$ shows that the motion includes limited hopping between close locations. The exponent ‘ s ’ depends on both the temperature and the nature of the material, but it is independent of the frequency [55]. The frequency-dependent change of conductivity at various temperatures shows that below the temperature T_{MS} (440 K for the two investigated

Table 2 The values of the force constants K_T obtained at room temperature for $\text{Mg}_{0.6}\text{Co}_{0.4}\text{FeCrO}_4$ ferrites sintered at 900 °C and 1100 °C

Sintering temperature	ν_A (cm^{-1})	$K_T \times 10^5$ (dyne/cm)	R_A (Å)
900 °C	582.876	1.445	1.961
1100 °C	597.383	1.518	1.957

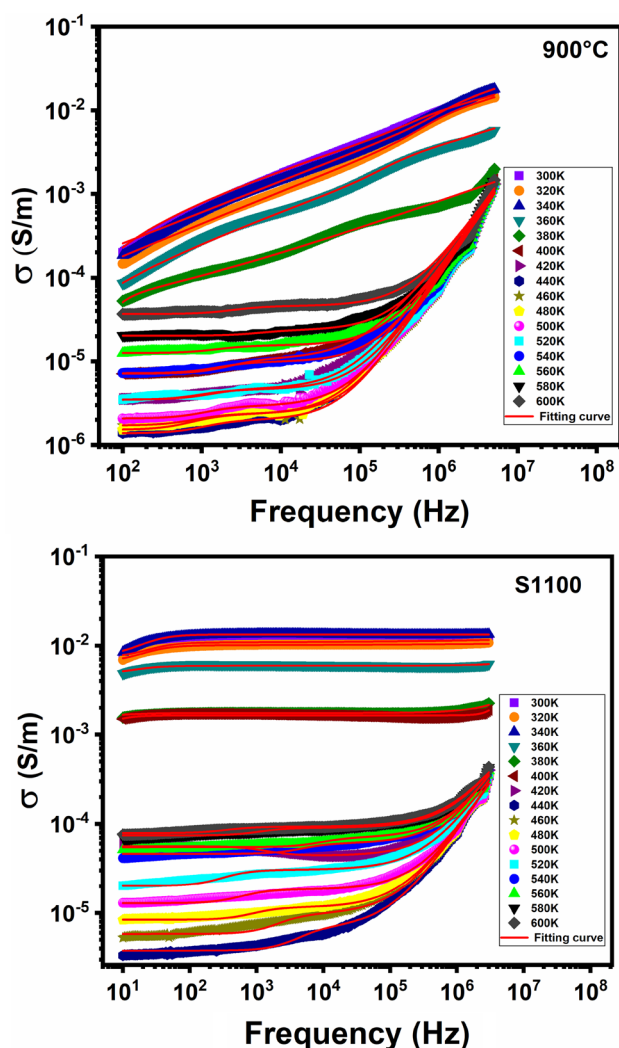


Fig. 5 Variation of electrical conductivity (σ) with frequency at various temperatures for $\text{Mg}_{0.6}\text{Co}_{0.4}\text{FeCrO}_4$ ferrites sintered at 900 °C and 1100 °C. Fit to experimental results is represented by red lines (Color figure online)

samples) the conductivity decreases with the frequency. This one demonstrates that the behavior of our samples is metallic [56]. Above the T_{MS} temperature, the conductivity increases with increasing frequency. In this case, our samples exhibit semiconductor behavior [57]. T_{MS} is therefore the transition temperature from metallic behavior to semiconductor behavior. The increase in conductivity with increasing frequencies is explained by the pumping force which allows charge carriers to be moved between different localized states while also allowing the trapped charges to be released from different trapping centers. These charge carriers, together with the electrons generated by the valence exchange of various metal ions, engage in conduction [58]. The experimental results of electrical conductivity shown in Fig. 5 are fitted according to Eq. (5). Symbols in this figure are the experimental data

and red lines are the best fits. It can be seen in this figure that there is a very good agreement between the experimental measurements and their adjustments using Eq. (5) over the entire frequency range. By studying the evolution of the exponent ‘s’ as a function of temperature, it is therefore necessary to examine the different results seen in the zone where the conductivity depends on ω^s . Figure 6a shows that the values of ‘s’ decrease until they reach a minimum and then increase. In this case, the most suitable model for describing the electrical conduction process in these materials is the Overlapping-Large Polaron Tunneling (OLPT) model. Beyond T_{MS} , the values of ‘s’ decrease as the temperature increases. We then deduce that the appropriate model to explain the transport properties in these materials is the Correlated Barrier Hopping (CBH) [59]. For the two samples sintered 900 °C and 1100 °C, the values of ‘s’ are greater than 1. This suggests that charge carrier hopping happens between two nearby sites [60]. Figure 6b illustrates the variation of the dc conductivity with temperature. We notice from this figure that for temperatures lower than T_{MS} , the values of σ_s decrease during the increase in temperature, then they increase when the temperature increases for temperatures above T_{MS} . These results clearly illustrate that our materials exhibit a metal–semiconductor transition at the T_{MS} temperature. It is also noticed that when the sintering temperature increases, the values of σ_s are increased in the whole explored temperature range and the T_{MS} does not change. This non-change of the transition temperature is in good agreement with other work [61]. The experimental results of the dc conductivity σ_s are fitted using the Arrhenius law by the following relation [62]:

$$\sigma_s = \sigma_0 \exp\left(-\frac{E_{\text{dc}}}{k_{\text{B}}T}\right) \quad (6)$$

where σ_0 is a pre-exponential factor, E_a represents the activation energy and k_{B} is the Boltzmann constant and T is the absolute temperature. Figure 6c displays the plots of $\text{Ln}(\sigma_s \times T)$ versus $(1000/T)$. For the two samples sintered at 900 °C and 1100 °C, the values of E_{dc} derived from the slope of the linear fitting plot are equal to 0.794 eV and 0.524 eV, respectively. The high E_{dc} value for the two samples investigated is owing to the high degree of disorder in these two samples induced by the large number of doping elements (Mg, Co, Cr) in these samples [63]. We can observe that the values of the activation energies decrease when the sintering temperature is high. This decrease in the activation energy means that the electrons during their jump, they require less energy. This one is due to the increase in the temperature of sintering. These different values of activation energies of our samples are lower than those obtained by other studies on ferrites compounds [63]. Therefore, these samples are classified as good conductors.

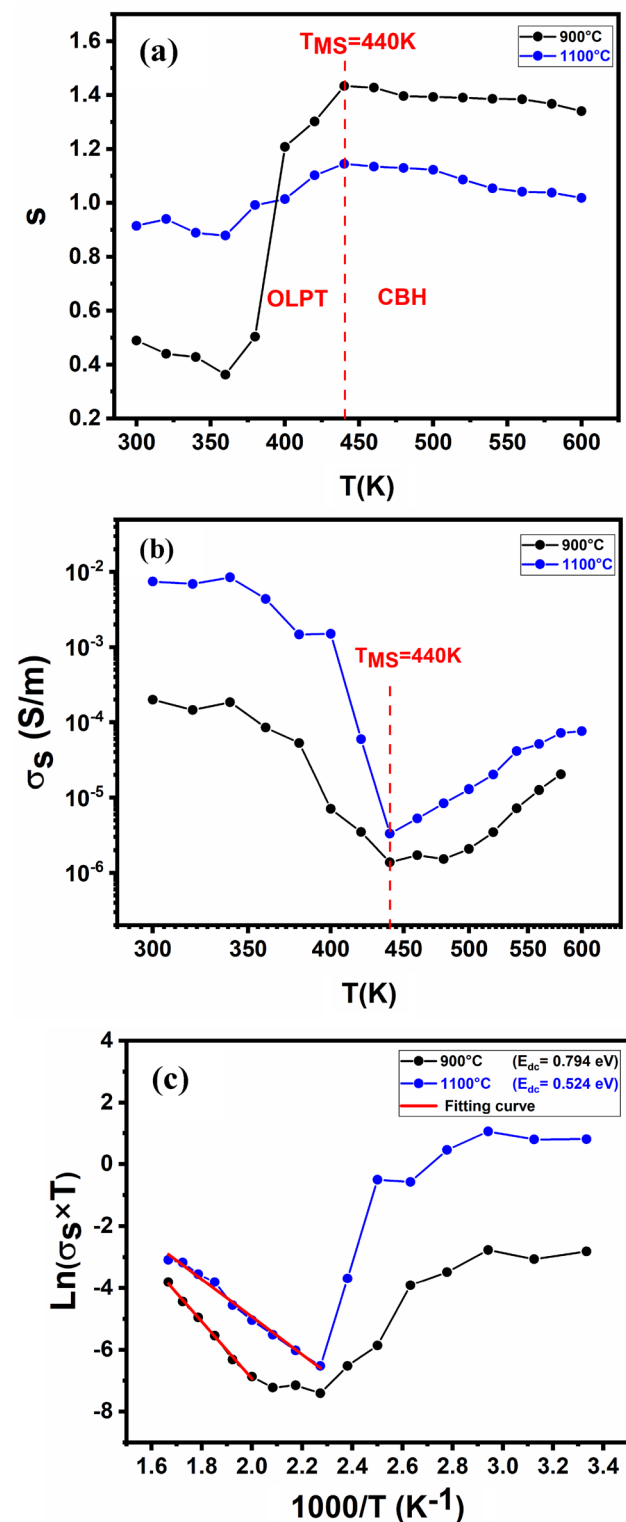


Fig. 6 a Variation of dc conductivity (σ_s) with temperature for $\text{Mg}_{0.6}\text{Co}_{0.4}\text{FeCrO}_4$ ferrites sintered at 900 °C and 1100 °C. **b** The temperature dependence of the exponent (s) for the two samples. **c** $\ln(\sigma_{dc} \times T)$ as a function of ($1000/T$) at a frequency of 100 Hz. Red lines represent the linear fit of conductivity data (Color figure online)

3.4 Dielectric Properties

The dielectric properties of ferrite nanoparticles are influenced by several factors including the synthesis technique, chemical composition, phase purity, crystal structure, the ratio of $\text{Fe}^{2+}/\text{Fe}^{3+}$, morphology, oxygen anion vacancies in lattices, cations distribution, frequency of the applied electric field, grain size and sintering temperature [64, 65]. The adaptation of these parameters makes it possible to obtain a material with the desired dielectric behavior. In this case, the dielectric response of the ferrite nanoparticles is considered as a complex quantity which is the complex permittivity, its expression is translated by the following formula $\epsilon^* = \epsilon' - j\epsilon''$, where (ϵ') and (ϵ'') respectively designate the real part and the imaginary part of the dielectric constant, with (ϵ') represents the stored energy and (ϵ'') designates the energy dissipated in the dielectric medium. The equation shown below is used to calculate the complex permittivity [66, 67]:

$$\epsilon^* = \frac{1}{j\omega C_0 Z^*} \quad (7)$$

where ω is the angular frequency, Z^* is the complex impedance spectroscopy of the sample and $C_0 = \epsilon_0 S/e$ represents its geometric capacity, with ϵ_0 represents the permittivity for free space. However, the real part (ϵ') and the imaginary part (ϵ'') of the dielectric constant as well as the dielectric loss tangent ($\tan \delta$) are determined using the equations shown below [68].

$$\epsilon' = \frac{Z''}{\omega C_0 (Z'^2 + Z''^2)} \quad (8)$$

$$\epsilon'' = \frac{Z'}{\omega C_0 (Z'^2 + Z''^2)} \quad (9)$$

$$\tan \delta = \frac{\epsilon''}{\epsilon'} \quad (10)$$

where $Z' = |Z|\cos\Phi$ and $Z'' = |Z|\sin\Phi$ are respectively the real part and the imaginary part of the complex impedance Z , and Φ is the argument defined as $\Phi = \frac{\pi}{2} - \delta$ where δ is the phase shift. Figures 7 and 8 illustrate, respectively, the variations of the real and imaginary parts of the dielectric constant as a function of frequency at different temperature for $\text{Mg}_{0.6}\text{Co}_{0.4}\text{FeCrO}_4$ ferrites sintered at 900 °C and 1100 °C. It is clear from the two exposed examples that the values of the real part (ϵ') and the imaginary part (ϵ'') of the dielectric constant are high at low frequency, and then they decrease as frequency increases, becoming extremely low in the high frequency zone. In this region the values of (ϵ') and (ϵ'') approach the same values and become independent of the frequency. Similar findings have been seen in other

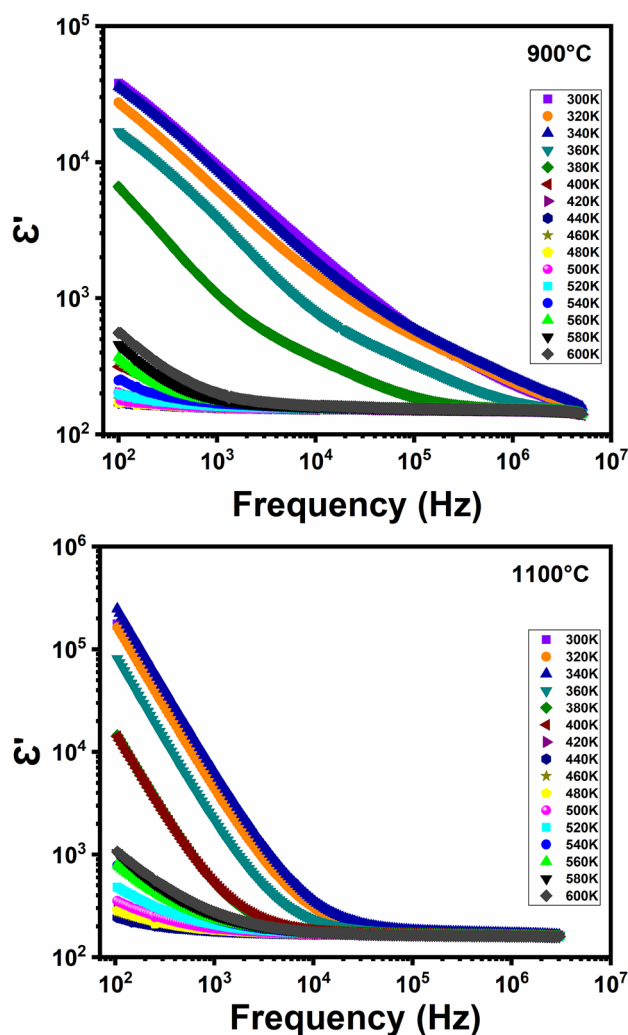


Fig. 7 Variations of ϵ' with frequency at various temperatures for $\text{Mg}_{0.6}\text{Co}_{0.4}\text{FeCrO}_4$ ferrites sintered at 900 °C and 1100 °C

studies [53, 69]. The dependence of the dielectric permittivity observed during the increase of frequency reflects that there is dielectric dispersion [70]. Dielectric dispersion with frequency in ferrite can be used to explain on the basis of Koop's theory [71] and Maxwell–Wagner interfacial type of polarization [72]. From to these theories, the ferrite material's dielectric structure may be thought of as a heterogeneous structure made of highly conductive grains and weakly conducting grain boundaries. Grain boundaries with low conductivity are considered useful at low frequencies, while grains with high conductivity are considered useful at high frequencies [73]. Under the effect of an applied alternating electric field, electric charges move in the grains and grain boundaries of the ferrite materials. Therefore, by application of the electric field, the movement of charges through grains and grain boundaries is interrupted at the grain boundaries and they exhibit accumulation of charges at the grain

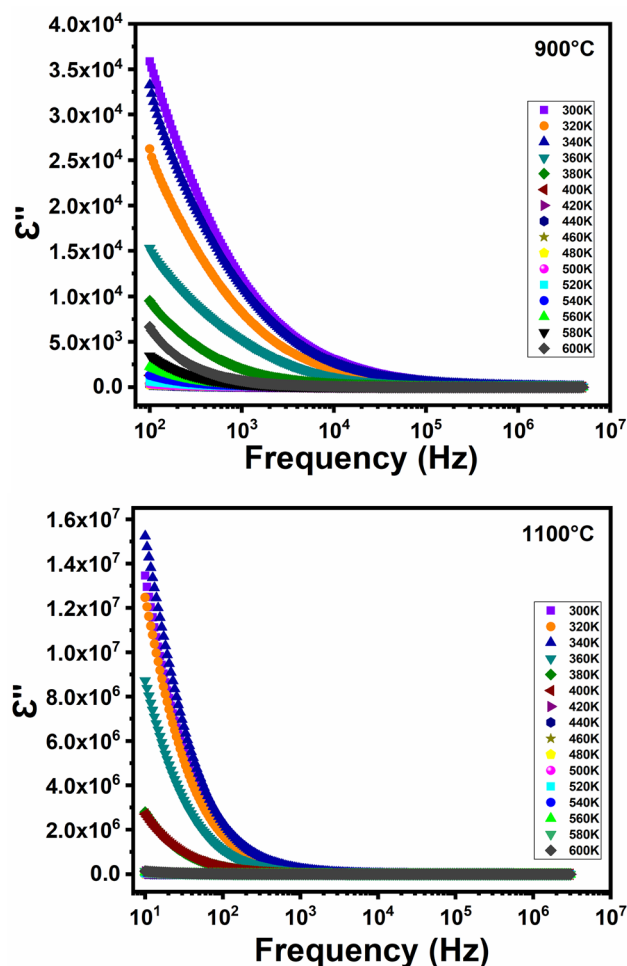


Fig. 8 Variations of ϵ'' with frequency at various temperatures for $\text{Mg}_{0.6}\text{Co}_{0.4}\text{FeCrO}_4$ ferrites sintered at 900 °C and 1100 °C

boundaries. Since the grain boundaries are very resistive, this accumulation of charges leads to an interfacial polarization [74]. Therefore, at low frequency, the dielectric constant has a high value. Moreover, when the frequency of the applied field increases, the exchange of electrons between the Fe^{2+} and Fe^{3+} ions does not follow the evolution of the external field applied at a certain frequency in the high frequency region. Consequently, the probability of reaching the grain boundary by the electrons decreases and this leads to a decrease in the interfacial polarization. Indeed, at high frequency, the dielectric constant becomes minimal and at the same time it does not depend on the frequency. As a result of the low dielectric constant values in the high frequency region, these samples are especially well suited for applications in this region [75]. With increasing sintering temperature, the diffuse and clumped atoms of ferrite compounds receive energy during sintering. This energy increases with increasing sintering temperature. As the energy increases, then more atoms clump together and therefore the size of

the crystals increases from 48 to 56 nm [76]. Furthermore, the larger crystallites size, the greater the contact between neighboring grains, then the movement of electrons will be easier, and they can flow easily to grain boundaries which leads to an increase in the polarization. Moreover, increasing the sintering temperature causes an increase in the generation of Fe^{2+} ions and hence the jumping process is stimulated. Similarly, the increase in temperature also releases more of the localized dipoles, which are therefore aligned by the applied electric field in its direction [77]. Consequently, raising the sintering temperature increases the dielectric polarization and therefore the permittivity increases [78]. Figure 9 displays the evolution of the dielectric loss tangent ($\tan\delta$) for $\text{Mg}_{0.6}\text{Co}_{0.4}\text{FeCrO}_4$ ferrites sintered at 900 °C and 1100 °C as a function of frequency at various temperatures. According to Fig. 9, the two samples exhibit relaxations in

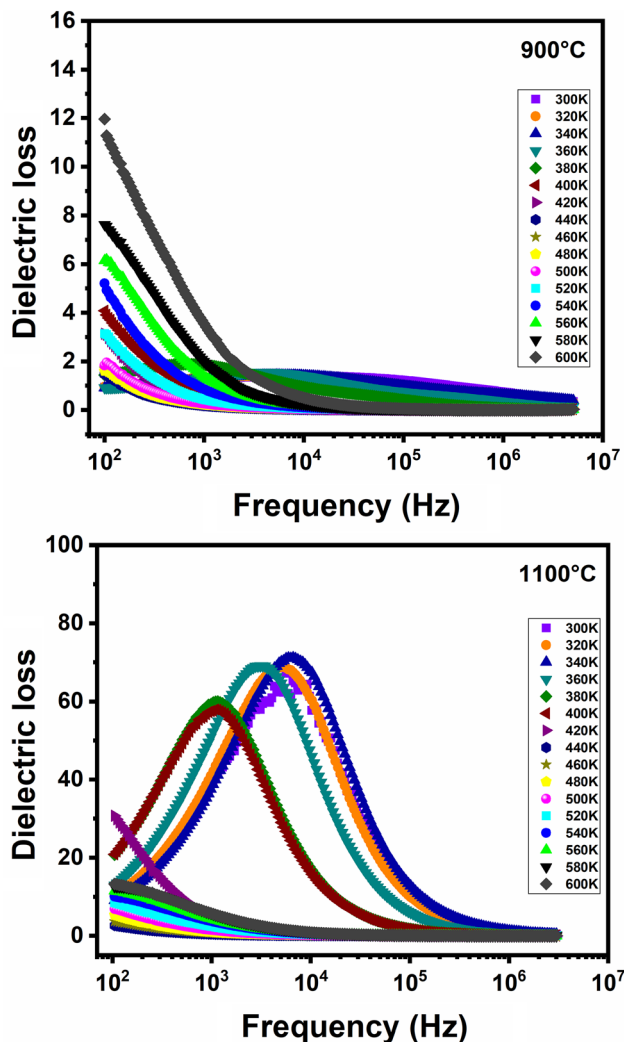


Fig. 9 Variations of the dielectric loss tangent ($\tan\delta$) with frequency at various temperatures for $\text{Mg}_{0.6}\text{Co}_{0.4}\text{FeCrO}_4$ ferrites sintered at 900 °C and 1100 °C

the metallic regime ($T < T_{\text{MS}}$), with a loss peak at specific frequencies appearing at lower frequencies and disappearing at higher frequencies. The loss peak is observed when the electron hopping frequency between Fe^{2+} and Fe^{3+} and the frequency of the established electric field are equal. The condition for having a resonance peak is given by the following relation [79]:

$$\omega\tau = 1 \quad (11)$$

where $\omega = 2\pi f$ represents the angular frequency, f is the frequency of the applied field and τ represents the relaxation time. According to Iwachi [80], the presence of the peak in the dielectric loss tangent ($\tan\delta$) as a function of frequency can be explained by the close link between the hopping conduction process and the dielectric behavior of ferrites. The loss peaks showed a shift to the high frequencies for both samples with high sintering temperatures. As the temperature drops, these peaks shift to a higher frequency at the same time. Moreover, it has been shown that increase in temperature is accompanied by a decrease in peak height. In the semiconductor regime ($T > T_{\text{MS}}$), the dielectric loss tangent ($\tan\delta$) of the two samples decreases at lower frequencies, then it becomes completely independent of frequency at higher frequencies. The loss is maximum when the frequency of the electric field applied is clearly lower than the frequency of the jump of electrons between the Fe^{2+} and Fe^{3+} ions on the neighboring octahedral sites and in this case the electrons obey the evolution of this electric field. It is minimal when the frequency of the electric field applied is greater than the jump frequency of electron exchange between the Fe^{2+} and Fe^{3+} ions and in this case the electrons do not obey the evolution of this electric field [81]. At low frequencies, the grain boundaries have low conductivity, so the charge carrier jump process requires more electrical energy, hence the loss is high. At high frequencies, the grain boundaries have high conductivity, so the charge carrier jumping process requires less electrical energy, hence the loss is low [82]. In this study, it can be deduced that the value of ($\tan\delta$) strongly depends on the sintering temperature.

3.5 Electric Modulus Analysis

The study of the complex dielectric modulus gives information on the nature of the polycrystalline samples, whether they are homogeneous or heterogeneous and also to have global ideas on the electrical relaxation process of a conducting material [83]. The adoption of a complex electrical modulus formalism aims to eliminate the electrode effect [84]. The following formula is employed to determine the complex modulus M^* [85]:

$$M^* = \frac{1}{\epsilon^*} = \frac{\epsilon'}{\epsilon'^2 + \epsilon''^2} + j \frac{\epsilon''}{\epsilon'^2 + \epsilon''^2} = M' + jM'' \quad (12)$$

where M' and M'' represent respectively the real and imaginary parts of the complex electrical module. Figure 10 depicts the variation of the real component M' of the modulus with frequency at various temperatures for $Mg_{0.6}Co_{0.4}FeCrO_4$ ferrites. It has been shown that the values of M' in the low frequency domain are extremely low, demonstrating that the polarization of the electrodes has little effect on the material [86]. It was found that the values of M' increased exponentially at intermediate frequencies. For high frequencies, we observe that the variation of the values of M' is independent of the frequency and that they tend towards a single value. This leads to the phenomenon of conduction due to the short-range mobility of charge carriers under the effect of the applied electric field [87, 88]. This leads to the conclusion that under the effect of the

applied electric field, the conduction phenomenon is due to the short-range mobility of the charge carriers.

Figure 11 shows the imaginary component of the complex electrical modulus M'' for $Mg_{0.6}Co_{0.4}FeCrO_4$ ferrites. We can see from this figure that the profile of the M'' curves at different temperatures is the same. The values of M'' initially increase with frequency until they reach their maximum value at (f_{max}). Then they begin to decrease as frequency increases. At different temperatures, the frequency-dependent spectra of M'' contain peaks that appear at specific frequencies (f_{max}). When the temperature falls below T_{MS} , the peaks shift to the high frequency band. However, once the temperature increases above T_{MS} , the peaks shift to the high frequency band. This suggests that these samples' dielectric relaxation is thermally activated. These peaks reveal an increasing frequency shift in the mobility of charge carriers from long-range to short-range. The frequency band below the peak maximum is the low frequency region. Charge carriers at this location

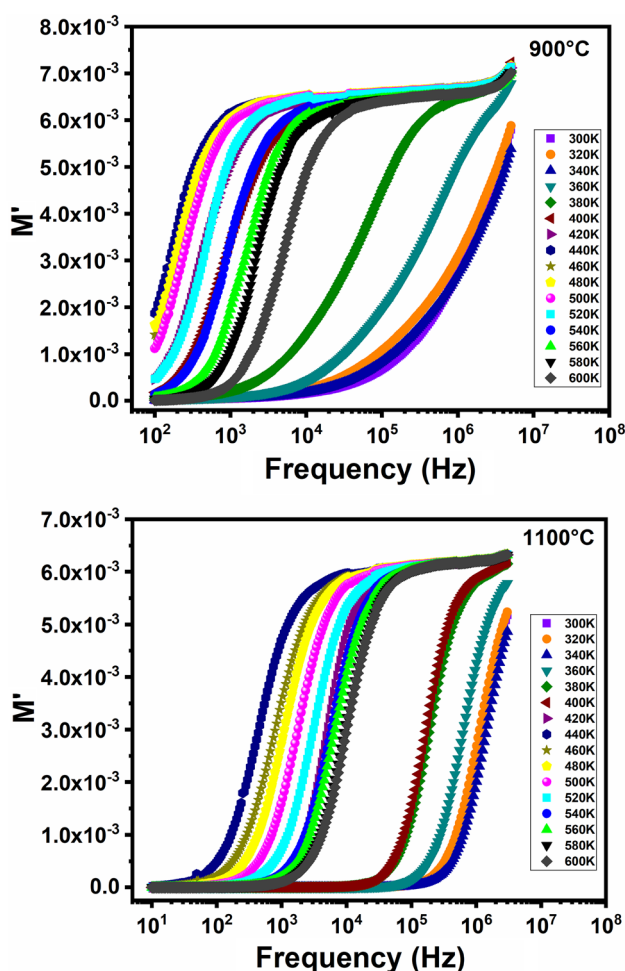


Fig. 10 Variations of M' with frequency at various temperatures for $Mg_{0.6}Co_{0.4}FeCrO_4$ ferrites sintered at 900 °C and 1100 °C

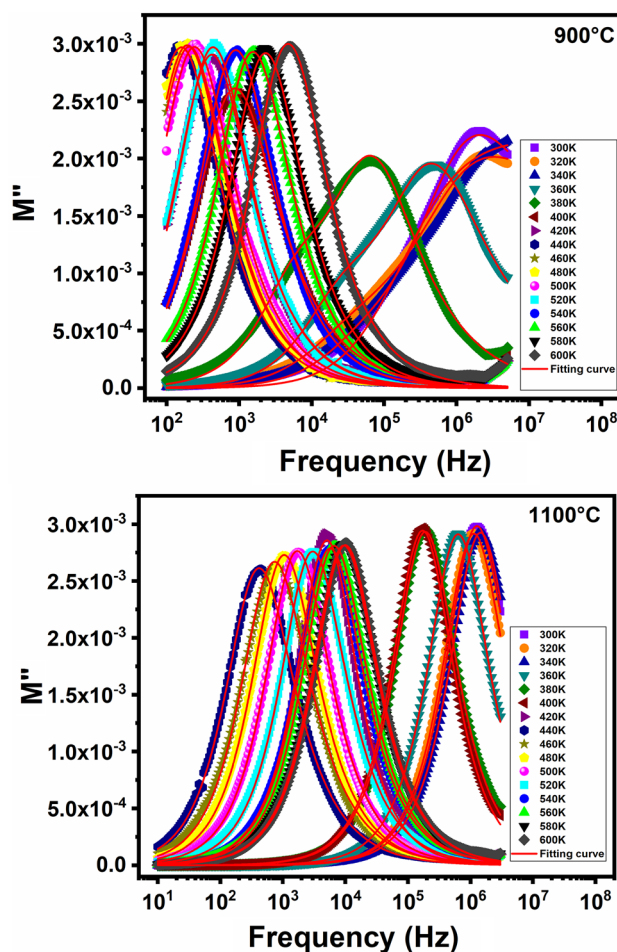


Fig. 11 Variations of M'' with frequency at various temperatures for $Mg_{0.6}Co_{0.4}FeCrO_4$ ferrites sintered at 900 °C and 1100 °C. Fit to experimental results is represented by red lines

can travel great distances. While the area of frequencies above the peak maxima is the high frequency area. In this zone, the charge carriers are spatially confined to their potential sinks, and they move over short distances [89]. The broadening asymmetry exhibited by the peaks at different temperatures shows that the propagation of relaxation times is with different time constants hence there is in these samples a non-Debye type of relaxation [90]. The following function is used to fit the curves of variation of M'' as a function of frequency at various temperatures [91]:

$$M'' = M''_{\max} / \left[1 - \beta + \left(\frac{\beta}{1 + \beta} \right) \left(\beta \left(\frac{f_{\max}}{f} \right) + \left(\frac{f}{f_{\max}} \right)^\beta \right) \right] \quad (13)$$

where M''_{\max} is the maximum of the peak, f_{\max} is its frequency and β is the stretching factor (varying from 0 to 1). This factor identifies the type of relaxation Debye or non-Debye that occurs in a particular material [92]. The parameters for adjusting the data of M'' as a function of frequency using Eq. (13) are given in Table 3. The values of β are less than one, as shown in this table, indicating that these samples exhibit non-Debye dielectric behavior [93]. The position of the peaks also makes it possible to obtain the relaxation time (τ) using this relation [94]:

$$\tau_{M''} = \frac{1}{2\pi f_{\max}} \quad (14)$$

Figure 12 shows the $\ln(\tau_{M''})$ vs. $(1000/T)$ curves which have also been modeled using the following Arrhenius relation [82, 95]:

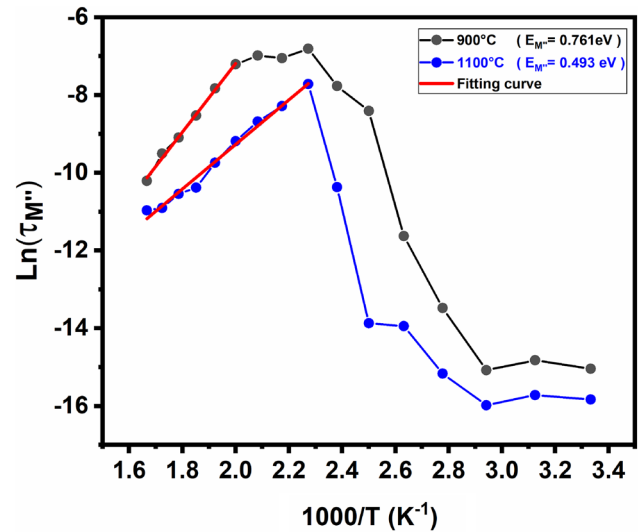


Fig. 12 Variation of the $\ln(\tau_{M''})$ as a function $(1000/T)$ for $Mg_{0.6}Co_{0.4}FeCrO_4$ ferrite sintered at 900 °C and 1100 °C. Fit to experimental results is represented by red lines (Color figure online)

$$\tau_{M''} = \tau_0 \exp\left(\frac{E_{M''}}{k_B T}\right) \quad (15)$$

with E_a being the activation energy, T being the temperature, k_B being the Boltzmann constant, and τ_0 being a pre-exponential factor. According to the linear adjustments of the curves, the activation energies $E_{M''}$ are 0.761 eV and 0.493 eV for the samples sintered at 900 °C and 1100 °C, respectively. The values of this energy are fairly close to those established by the investigation of dc conductivity σ_s . Figure 13 depicts Cole–Cole plots for $Mg_{0.6}Co_{0.4}FeCrO_4$

Table 3 Fitting parameters derived from the experimental data of imaginary part of modulus versus frequency at different temperatures for $Mg_{0.6}Co_{0.4}FeCrO_4$ ferrites sintered at 900 °C and 1100 °C

T(K)	900 °C				1100 °C			
	$M''_{\max} \times 10^{-4}$	β	$f_{\max} \times 10^3$ (Hz)	χ^2	$M''_{\max} \times 10^{-4}$	β	$f_{\max} \times 10^3$ (Hz)	χ^2
300	35.6	0.309	542.665	0.972	34.5	0.893	1195.870	1
320	32.3	0.312	434.381	0.977	33.6	0.895	1066.160	0.999
340	32.8	0.345	210.656	0.982	32.9	0.916	972.991	0.999
360	26.7	0.178	54.891	0.959	32	0.933	613.430	0.999
380	32.6	0.409	17.818	0.934	32.9	0.916	48.118	0.999
400	36.6	0.702	5.104	0.996	30.9	0.967	168.293	0.999
420	36.5	0.819	0.376	0.997	28.5	0.998	5.059	0.997
440	36.9	0.828	0.143	0.996	34.8	0.758	0.356	0.998
460	37.1	0.826	0.184	0.997	35.6	0.757	0.629	0.998
480	37.5	0.819	0.171	0.996	34.5	0.812	0.936	0.998
500	37.7	0.808	0.214	0.997	34	0.839	1.550	0.999
520	36.2	0.848	0.399	0.997	34.6	0.822	2.699	0.999
540	37.2	0.815	0.801	0.997	34.5	0.832	5.149	0.999
560	35.9	0.843	1.411	0.997	34.3	0.846	6.031	0.999
580	35.1	0.858	2.136	0.997	34.1	0.853	8.649	0.999
600	36.7	0.842	4.315	0.996	33.9	0.859	9.220	0.999

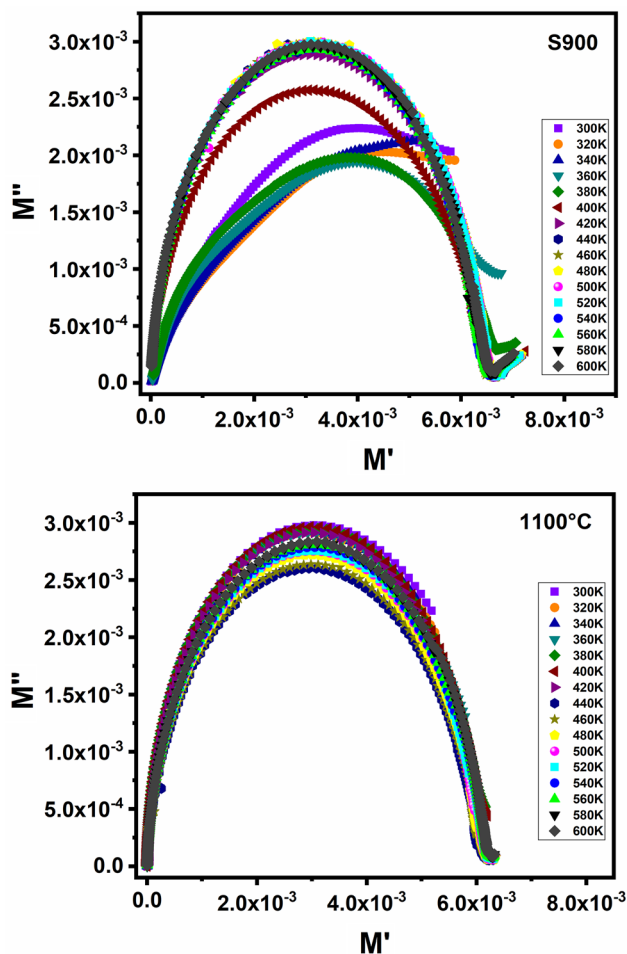


Fig. 13 Complex modulus spectra at different temperatures for $Mg_{0.6}Co_{0.4}FeCrO_4$ ferrites sintered at 900 °C and 1100 °C

ferrites at various temperatures. We can notice from Cole–Cole plots that the patterns are characterized by the presence of little asymmetric. This suggests that these samples exhibit electrical relaxation phenomena [96].

3.6 Complex Impedance Analysis

The evolution of the real component of the impedance Z' with frequency at various temperatures is shown in Fig. 14. It can be seen from this figure that for temperatures above T_{MS} , the values of Z' are high in the low frequency band, then they increase when the frequency increases. Below T_{MS} , they decrease with decreasing temperature. This suggests that the ac conductivity increased with increasing temperature and frequency [95]. This phenomenon could be explained by an increase in the mobility of charge carriers and a decrease in the density of confined charges [73]. At high frequencies, the Z' values at all temperatures begin to converge. This phenomenon can be explained by the existence of space charge polarization [60]. It's important to

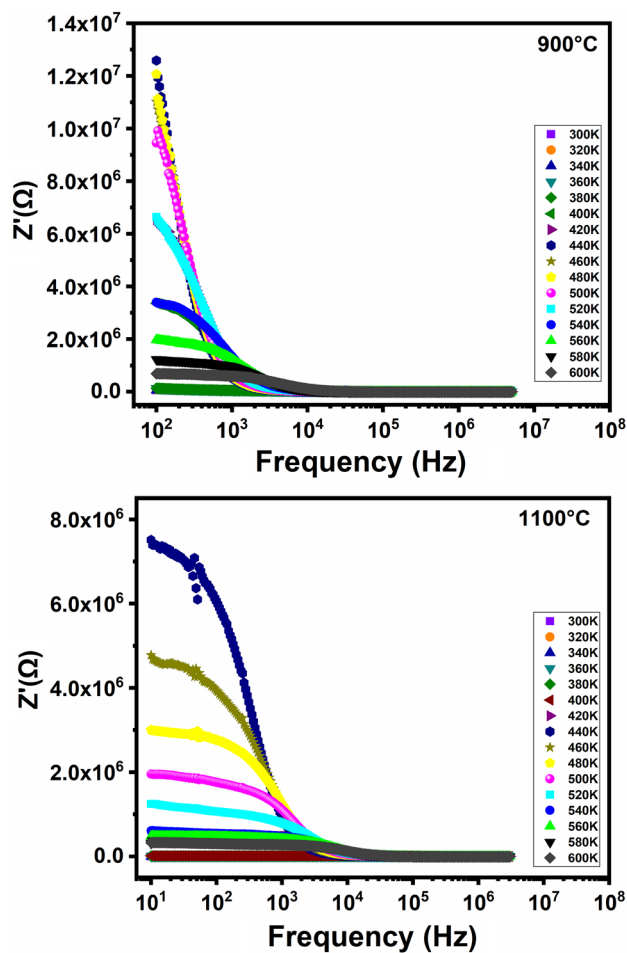


Fig. 14 Variations of Z' with frequency at various temperatures for $Mg_{0.6}Co_{0.4}FeCrO_4$ ferrites sintered at 900 °C and 1100 °C

also mention that Z' decreased as the sintering temperature increases. Other studies on ferrite compounds have shown a comparable variation in Z' [47, 97]. The decrease in Z' values indicates that the resistive properties of samples have decreased. This phenomenon is caused by the existence of space charge polarization in the samples [98].

The variation of the imaginary component Z'' of impedance with frequency at various temperatures is depicted in Fig. 15. It can be shown that, for temperatures over T_{MS} , the spectra of Z'' are characterized by the presence of sharp peaks that, as temperature rises, travel closer to the high-frequency zone. This indicates that a relaxation phenomenon exists in these samples [55] and that these relaxations are thermally activated [99]. But for temperatures below T_{MS} , these peaks shift to the high frequency region as the temperature decreases. This behavior can be also attributed to the fact that the polarization establishment time (i.e., the relaxation time) in the metallic region increases with increasing temperature; however, in the semiconductor region the relaxation time decreases. In addition, at higher frequencies,

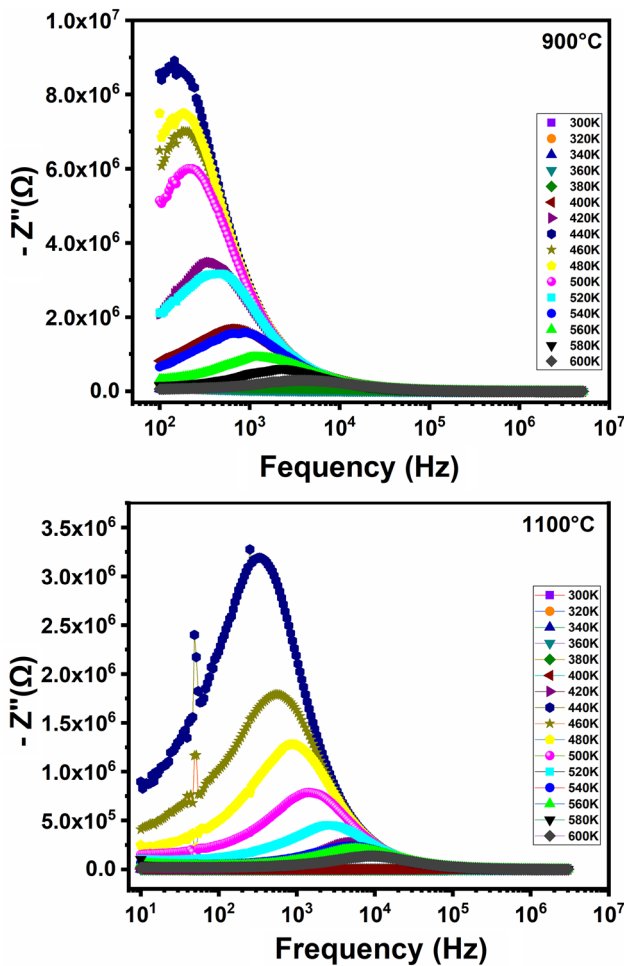


Fig. 15 Variations of Z'' with frequency at various temperatures for $Mg_{0.6}Co_{0.4}FeCrO_4$ ferrites sintered at 900 °C and 1100 °C

all the curves Z'' coincide; this phenomenon is caused by the accumulation of space charge in these compounds [100, 101]. It is also noted that for these two samples sintered at 900 °C and at 1100 °C, that at different temperatures, the values of Z'' increases when increasing the frequency, but for a certain frequency, these values gradually decrease which is due to the decrease in the polarization which does not follow the frequency of the alternating electric field applied [48]. In this instance, we also observed that the relaxation peaks migrated into the high frequency region as the sintering temperature increases. This behavior demonstrates that when the sintering temperature rises, the relaxation time shortens and the mobility of the hopping charge carriers rises, which results in a loss of material strength [101].

Figure 16 shows the Nyquist plots at various temperatures for $Mg_{0.6}Co_{0.4}FeCrO_4$ ferrites. Two arcs of circles that are not centered on the real axis can be seen in the impedance spectra, which may indicate non-Debye relaxation [65]. The first arc, which is a complete semicircle, is seen at high

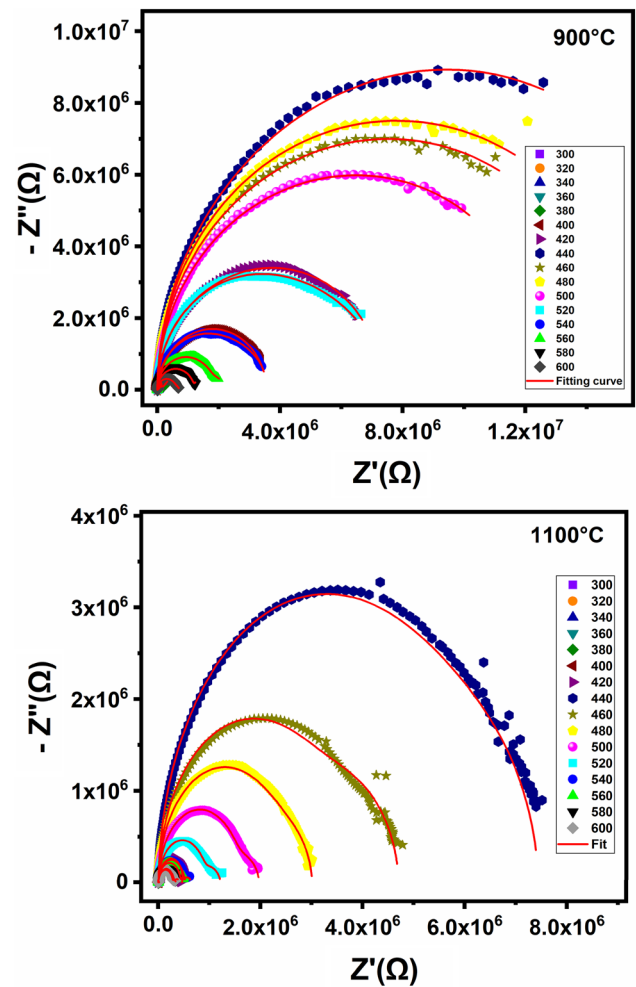


Fig. 16 Nyquist curves at various temperatures of $Mg_{0.6}Co_{0.4}FeCrO_4$ ferrites sintered at 900 °C and 1100 °C

frequencies, but the second arc, which is an incomplete semicircle with a larger radius, is seen at low frequencies. This second arc corresponds to the contribution of the grain boundary resistance (R_{gb}), whereas the first arc denotes the contribution of the grain [102]. The two arcs seen in the impedance spectra suggest the presence of two types of relaxation [103]. From the spectra, it is observed that for temperatures above T_{MS} , half-arc radii decrease as temperature increases. The reduction in half-arc radii as temperature increases proves that electrical conductivity increases as temperature increases [104].

Zview software is used to fit impedance data for all temperatures [69]. Red lines in Fig. 16 represent the appropriate fit, is made using an equivalent circuit composed of a serial association of two contributions which is represented in the Fig. 17 [69]. The interpretation of the impedance spectra has been based on the first contribution, which is related to the grains (R_g-CPE_g), and the second contribution, which is related to the grain boundaries ($R_{gb}-CPE_{gb}$), where R_g and

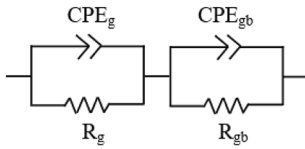


Fig. 17 The equivalent circuit used for the analysis of the impedance data

R_{gb} denote grain and grain boundary resistance respectively, and CPE_g and CPE_{gb} denote grain and grain boundary constant phase elements respectively.

The following equation determines the impedance of a CPE [45]:

$$Z_{CPE} = \frac{1}{Q(j\omega)^\alpha} \tag{16}$$

where ω is the angular frequency, Q denotes the capacitance value of the CPE element and α are frequency independent parameters. The real and imaginary parts of the impedance are determined using the following formulas [105]:

$$Z' = \frac{R_g + R_g^2 Q_g \omega^{\alpha_g} \cos(\alpha_g \frac{\pi}{2})}{[1 + R_g Q_g \omega^{\alpha_g} \cos(\alpha_g \frac{\pi}{2})]^2 + [R_g Q_g \omega^{\alpha_g} \sin(\alpha_g \frac{\pi}{2})]^2} + \frac{R_{gb} + R_{gb}^2 Q_{gb} \omega^{\alpha_{gb}} \cos(\alpha_{gb} \frac{\pi}{2})}{[1 + R_{gb} Q_{gb} \omega^{\alpha_{gb}} \cos(\alpha_{gb} \frac{\pi}{2})]^2 + [R_{gb} Q_{gb} \omega^{\alpha_{gb}} \sin(\alpha_{gb} \frac{\pi}{2})]^2} \tag{17}$$

$$-Z'' = \frac{R_g^2 Q_g \omega^{\alpha_g} \sin(\alpha_g \frac{\pi}{2})}{[1 + R_g Q_g \omega^{\alpha_g} \cos(\alpha_g \frac{\pi}{2})]^2 + [R_g Q_g \omega^{\alpha_g} \sin(\alpha_g \frac{\pi}{2})]^2} + \frac{R_{gb}^2 Q_{gb} \omega^{\alpha_{gb}} \sin(\alpha_{gb} \frac{\pi}{2})}{[1 + R_{gb} Q_{gb} \omega^{\alpha_{gb}} \cos(\alpha_{gb} \frac{\pi}{2})]^2 + [R_{gb} Q_{gb} \omega^{\alpha_{gb}} \sin(\alpha_{gb} \frac{\pi}{2})]^2} \tag{18}$$

Table 4 displays the values of all the fitted parameters. This table shows that at temperatures lower than T_{MS} , the grain boundary resistance R_{gb} , the grain boundary R_g and the total resistance ($R = R_g + R_{gb}$) increase with temperature, which confirms the metallic behavior of these compounds, but at temperatures above T_{MS} these resistances decrease with temperature; this confirms the semiconductor behavior of this compound. The observed decrease can be attributed to the grain boundary effect, which reduced the barrier to charge carrier hopping [94]. It has been observed that at different temperatures the resistances of R_{gb} grains have higher values than that of R_g grains. It is because of the atomic arrangement, which is disordered near the grain boundary, causing a marked increase in electron scattering [55, 106]. As a consequence, we may conclude that the grain boundary contribution is mostly responsible for the conduction mechanism in the samples. It should be observed that the R_g and R_{gb} values are higher for the sample sintered at 900 °C than for that sintered at 1100 °C. Figure 18 shows the logarithmic evolution of the total resistance (R) for the two samples as a function of the inverse of the temperature. The

Table 4 Electrical parameters obtained from Nyquist plots at different temperatures for $Mg_{0.6}Co_{0.4}FeCrO_4$ ferrites sintered at 900 °C and 1100 °C

ST (°)	900 °C			1100 °C		
	$R_g \times 10^4 (\Omega)$	$R_{gb} \times 10^4 (\Omega)$	$R \times 10^4 (\Omega)$	$R_g \times 10^4 (\Omega)$	$R_{gb} \times 10^4 (\Omega)$	$R \times 10^4 (\Omega)$
300	1.325	60.665	61.99	0.288	3.26	3.548
320	1.73	65.084	66.814	0.247	3.154	3.401
340	1.891	62.489	64.38	0.389	2.616	3.005
360	3.126	86.654	89.78	0.418	3.513	3.931
380	12.837	110.586	123.423	1.446	5.001	6.447
400	153.21	325.421	478.421	1.519	4.828	6.347
420	189.6	545.43	735.03	12.881	33.852	46.733
440	499.71	1328.7	1828.41	213.57	559.39	772.96
460	482.43	895.25	1377.68	156.21	314.06	470.27
480	407.46	789.8	1197.26	68.959	232.12	301.079
500	374.9	695.89	1070.79	42.834	154.5	197.334
520	229.88	507.91	737.79	32.104	89.606	121.71
540	100.28	259.26	359.54	14.854	49.634	64.488
560	41.28	179.6	220.28	12.124	43.053	55.177
580	30.421	117.22	147.641	11.923	30.26	42.183
600	11.61	59.693	71.303	6.645	27.832	34.477

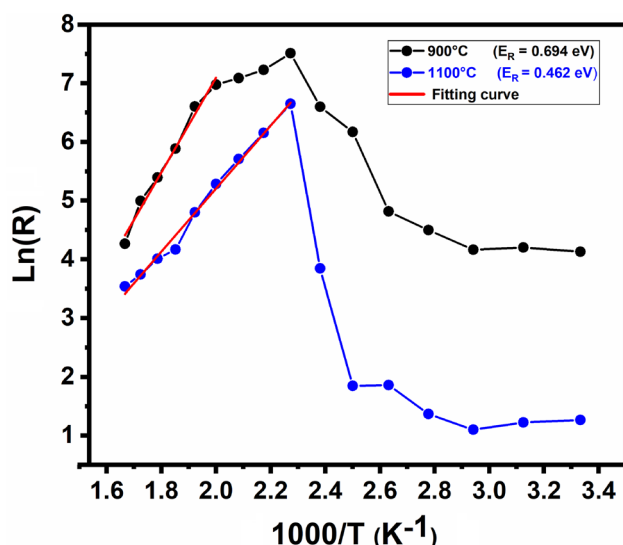


Fig. 18 Variation of $\text{Ln}(R)$ versus $(1000/T)$ for $\text{Mg}_{0.6}\text{Co}_{0.4}\text{FeCrO}_4$ ferrites sintered at 900 °C and 1100 °C. Fit to experimental results is represented by red lines (Color figure online)

activation energy is determined from the following Arrhenius' law [99]:

$$R = R_0 \exp\left(\frac{E_R}{k_B T}\right) \quad (19)$$

where k_B represents the Boltzmann constant, R_0 is a pre-exponential term and E_a is the activation energy. For $T > T_{MS}$, the curves in Fig. 18 are fitted by red lines using Eq. (19); from which the values of the activation energies of these samples will be determined. For the sample sintered at 900 °C, the activation energy is $E_R = 0.462$ eV and that for the sample sintered at 1100 °C is $E_R = 0.462$ eV. These results are similar to those obtained via the study of dc conductivity σ_s .

4 Conclusion

In conclusion, we investigated the structural, infrared, and electrical properties of $\text{Mg}_{0.6}\text{Co}_{0.4}\text{FeCrO}_4$ ferrites synthesized by the sol gel process and sintered at 900 °C and 1100 °C. According to X-ray diffraction measurements, our samples crystallize in the cubic structure with the space group $\text{Fd}\bar{3}m$. In FTIR spectra, only peaks associated with tetrahedral stretching are observable. The increase in sintering temperature was accompanied by an increase in cell parameters, crystallites size, absorption bands, conductivity, dielectric constants, and dielectric loss tangent. A semiconductor–metal transition is observed in the tow samples at a specific temperature T_{MS} . We observed that the T_{MS} is not

affected by the sintering temperature. The conduction process for the two samples follows both the NSPT and CBH models. The values of dielectric constants decrease gradually as frequency increases. The decrease in dielectric constants as frequency increases is interpreted by Koop's theory and the Maxwell–Wagner type of interfacial polarization. The variation of the imaginary components of modulus and impedance suggests that both samples exhibit non-Debye dielectric relaxation. The Nyquist curves are adjusted using an equivalent circuit composed of a series association of two circuits $[(R_{gb} // CPE_{gb}) \text{ and } (R_g // CPE_g)]$. The estimated activation energies derived from the electrical modulus spectrum, impedance, and dc conductivity analyses are found to be quite similar, suggesting that the phenomenon of relaxation process and electrical conduction are both related to the same defect.

Author contributions All authors certify that they have participated sufficiently in the work to take public responsibility for the content, including participation in the concept, analysis, design, and writing. The final manuscript was read and approved by all authors.

Funding The authors have not disclosed any funding.

Data availability Upon a reasonable request, the data that support this study's findings are available from the corresponding author.

Declarations

Conflict of interest The authors have no competing interests that are relevant to the content of this article to declare.

References

1. A. Khan, P. Chen, P. Boolchand, P.G. Smirniotis, *J. Catal.* **253**, 91–104 (2008)
2. D.S. Mathew, R.S. Juang, *Chem. Eng. J.* **129**, 65 (2007)
3. S.A. Kumar, R. Kumar, P. Thakur, K.H. Chae, B. Angadi, W.K. Choi, *J. Phys. Condens. Matter* **19**, 476210 (2007)
4. G. Sathishkumar, C. Venkataraju, K. Sivakumar, *Mater. Sci. Appl.* **1**, 19–24 (2010)
5. S. Ayyappan, S. Mahadevan, P. Chandramohan, M.P. Srinivasan, J. Philip, B. Raj, *J. Phys. Chem. C* **114**, 6334–6341 (2010)
6. J. Li, H. Yuan, G. Li, Y. Liu, J. Leng, *J. Magn. Magn. Mater.* **322**, 3396–3400 (2010)
7. S. Choudhury, B.M. Alam, S.M. Hoque, *Int. Nano Lett.* **1**, 111–116 (2011)
8. S. Chakrabarty, M. Pal, A. Dutta, *Mater. Chem. Phys.* **153**, 221–228 (2015)
9. E. Mazarío, P. Herrasti, M.P. Morales, N. Menéndez, *Nanotechnology* **23**, 355708 (2012)
10. A. Safari, Kh. Gheisari, M. Farbod, *J. Magn. Magn. Mater.* **488**, 165369 (2019)
11. S. Rahman, K. Nadeem, M. Anis-ur-Rehman, M. Mumtaz, S. Naeem, I. Letofsky-Papst, *Ceram. Int.* **39**, 5235 (2013)
12. K. Chen, L. Jia, X. Yu, H. Zhang, *J. Appl. Phys.* **115**, 17A520 (2014)

13. Li, Sun, R. Zhang, Q. Ni, E. Cao, W. Hao, Y. Zhang, L. Ju, *Physica B* **545**, 4 (2018)
14. C. Singh, S. Jauhar, V. Kumar, J. Singh, S. Singhal, *Mater. Chem. Phys.* **156**, 188 (2015)
15. I. Soibam, S. Phanjoubam, C. Prakash, *J. Alloys Compd.* **475**, 328 (2009)
16. M. Naeema, N.A. Shahb, I.H. Gul, A. Maqsood, *J. Alloys Compd.* **487**, 739–743 (2009)
17. M.J. Iqbal, Z. Ahmad, T. Meydan, Y. Melikhov, *J. Appl. Phys.* **111**, 033906 (2012)
18. S. Supriya, S. Kumar, R. Pandey, L.K. Pradhan, M. Kar, *AIP Conf Proc.* **1953**, 050070 (2018)
19. S.A. Chambers, R.F.C. Farrow, S. Maat, M.F. Toney, L. Folks, J.G. Catalano, T.P. Trainor, G.E. Brown Jr., *J. Magn. Magn. Mater.* **246**, 124–139 (2002)
20. M.C. Terzzoli, S. Duhalde, S. Jacobo, L. Steren, C. Moína, *J. Alloys Compd.* **369**, 209–212 (2004)
21. S.G. Kakade, Y.R. Ma, R.S. Devan, Y.D. Kolekar, C.V. Ramana, *J. Phys. Chem. C* **120**, 5682–5693 (2016)
22. M. Grigorova, H.J. Blythe, V. Blaskov, V. Rusanov, V. Petkov, V. Masheva, D. Nihitjanova, L.M. Martinez, J.S. Muñoz, M. Mikhov, *J. Magn. Magn. Mater.* **183**, 163–172 (1998)
23. S.Y. Mulushoa, M.T. Wegayehu, G.T. Aregai, N. Murali, M.S. Reddi, B.V. Babu, T. Arunamani, K. Samatha, *Chem Sci Trans.* **6**, 653–661 (2017)
24. S. Verma, P.A. Joy, Y.B. Kholam, H.S. Potdar, S.B. Deshpande, *Mater. Lett.* **58**, 1092–1095 (2004)
25. S. Balamurugan, R. Ragasree, B.C. Brightlin, T.S. Gokul Raja, *J. Clust. Sci.* **33**, 547–555 (2022)
26. A.M. Gismelseed, K.A. Mohammed, M.E. Elzain, H.M. Widatalah, A.D. Al-Rawas, A.A. Yousif, *Hyperfine Interact* **208**, 33–37 (2012)
27. P.P. Hankare, V.T. Vader, N.M. Patil, S.D. Jadhav, U.B. Sankpal, M.R. Kadam, B.K. Chougule, N.S. Gajbhiye, *Mater. Chem. Phys.* **113**, 233–238 (2009)
28. I.A. Abdel-Latif, H.M. Zaki, *Mater. Chem Phys.* **275**, 125256 (2022)
29. G.S.N. Rao, B.P. Rao, H.H. Hamdeh, *Procedia Mater. Sci.* **6**, 1511–1515 (2014)
30. D. Gingasu, L. Diamandescu, I. Mindru, G. Marinescu, D.C. Culita, J.M. Calderon-Moreno, S. Preda, C. Bartha, L. Patron-Croat, *Chem. Acta* **88**, 445–451 (2015)
31. A.T. Raghavender, K.M. Jadhav, *Bull. Mater. Sci.* **32**, 575–578 (2009)
32. U.G. Akpan, B.H. Hameed, *Appl. Catal. A* **375**, 1–11 (2010)
33. U. Wongpratad, S. Maensiri, E. Swatsitang, *Ceram. Int.* **43**, 351 (2017)
34. R.N. Bhowmik, G. Vijayasri, *J. Phys. Appl. Phys.* **114**, 223701 (2013)
35. M.A. Ahmed, A.A. EL-Khawlani, *J. Magn. Magn. Mater.* **321**, 1959 (2009)
36. R.D. Shannon, *Acta Cryst. A* **32**, 751 (1976)
37. M.S. Anwar, F. Ahmed, B.H. Koo, *Acta. Mater.* **71**, 100–107 (2014)
38. P. Scherrer, *K. Nachr. Ges. Wiss. Goettingen, Math.-Phys. Kl* **26**, 98 (1918)
39. J.I. Langford, A.J.C. Wilson, *J. Appl. Cryst.* **11**, 102 (1978)
40. M.S. AlKathy, R. Gayam, K.C.J. Raju, *J. Ceram. Int.* **42**, 15432–15441 (2016)
41. K. Mohan, Y.C. Venudhar, *J. Mater. Sci. Lett.* **18**, 13–16 (1999)
42. M. Sassi, A. Oueslati, M. Gargouri, *Appl. Phys. A.* **119**, 763–771 (2015)
43. V.M. Khot, A.B. Salunkhe, M.R. Phadatare, S.H. Pawar, *Chem. Phys.* **132**, 782 (2012)
44. E. AlArfaj, S. Hcini, A. Mallah, M.H. Dhaou, M.L. Bouazizi, *J. Supercond. Nov. Magn.* **31**, 4107 (2018)
45. H. Huili, B. Grindi, A. Kouki, G. Viau, L.B. Tahar, *Ceram. Int.* **41**, 6212–6225 (2015)
46. A.N. Kumar, P. Kuruva, C. Shivakumara, C. Srilakshmi, *Inorg. Chem.* **53**, 12178–12185 (2014)
47. M.D. Rahaman, M.D. Mia, M.N.I. Khan, A.K.M.A. Hossain, *J. Magn. Magn. Mater.* **404**, 238 (2016)
48. S. Nasrin, S.M. Khan, M.A. Matin, M.N.I. Khan, A.K.M. Akther Hossain, M.D. Rahaman, *J. Mater. Sc. Mater. Electron* **30**, 10722–10741 (2019)
49. S. Kumar, S.K. Sharma, S. Rajpal, S.R. Kumar, S. Sahu, D. Roy, *Inter. J. Adv. Eng. Res. Sci.* **3**, 63 (2016)
50. Y. Liu, Y. Zhang, J.D. Feng, C.F. Li, J. Shi, R. Xiong, *J. Exp. Nano Sci.* **4**, 159 (2009)
51. C.V. Reddy, S.V.P. Vattikuti, R.V.S.S.N. Ravikumar, S.J. Moon, J. Shim, *J. Magn. Magn. Mater.* **394**, 70–76 (2015)
52. F. Hcini, S. Hcini, B. Alzahrani, S. Zemni, M.L. Bouazizi, *Appl. Phys. A.* **126**, 362 (2020)
53. N. Kouki, S. Hcini, R. Aldaowas, M. Boudard, *J. Supercond. Nov. Magn.* **32**, 2209 (2019)
54. C. Ben Mohamed, K. Karoui, S. Saidi, K. Guidara, A. Ben Rhaïem, *Physica B* **451**, 87–95 (2014)
55. A. Selmi, S. Hcini, H. Rahmouni, A. Omri, M.L. Bouazizi, A. Dhahri, *J. Phase Transit.* **90**, 942–954 (2017)
56. N. Assoudi, W. Hzez, R. Dhahri, I. Walha, H. Rahmouni, K. Khirouni, E. Dhahri, *J. Mater. Sci. Mater. Electron.* **29**, 20113 (2018)
57. M. Abdullah Dar, K.M. Batoo, V. Verma, W.A. Siddiqui, R.K. Kotnala, *J. Alloys Compd.* **493**, 553 (2010)
58. M.A. Ahmed, E. Ateia, S.I. El-Dek, *J. Mater. Lett.* **57**, 4256 (2003)
59. M.F. Kotkata, F.A. Abdel-Wahab, H.M. Maksoud, *J. Phys. D. Appl. Phys.* **39**, 2059 (2006)
60. M.H. Dhaou, S. Hcini, A. Mallah, M.L. Bouazizi, A. Jemni, *Appl. Phys. A* **123**, 8 (2017)
61. H. Baaziz, N.K. Maaloul, A. Tozri, H. Rahmouni, S. Mizouri, K. Khirouni, E. Dhahri, *Chem. Phys. Lett.* **640**, 77–81 (2015)
62. W. Hizi, H. Rahmouni, M. Gassoumi, K. Khirouni, S. Dhahri, *Eur. Phys. J. Plus* **135**, 456 (2020)
63. S.K. Mandal, S. Singh, P. Dey, J.N. Roy, P.R. Mandal, T.K. Nath, *J. Alloys Compd.* **656**, 887 (2016)
64. I.H. Gul, A. Maqsood, *J. Alloys Compd.* **465**, 227–231 (2008)
65. K. Akhtar, M. Gul, I.U. Haq, S.S.A. Shah, Z.U. Khan, *J. Inorg. Nano-Met. Chem.* **47**, 1722–1727 (2017)
66. N. Hamdaoui, Y. Azizian-Kalandaragh, M. Khelifi, L. Beji, *Ceram. Int.* **45**, 16458–16465 (2019)
67. H.M.T. Farid, I. Ahmad, I. Ali, A. Mahmood, S.M. Ramay, *Eur. Phys. J. Plus* **41**, 133 (2018)
68. M. Srivastava, R.K. Mishra, J. Singh, N. Srivastava, N.H. Kim, J.H. Lee, *J. Alloys Compd.* **645**, 171–177 (2015)
69. H. Chouaibi, J. Khelifi, A. Benali, E. Dhahri, M.A. Valente, A. Koumina, *J. Alloys Compd.* **839**, 155601 (2020)
70. C.V. Ramana, Y.D. Kolekar, K. Kamala Bharathi, B. Sinha, K. Ghosh, *J. Appl. Phys.* **114**, 183907 (2013)
71. C.G. Koops, *Phys. Rev.* **83**, 121–124 (1951)
72. K.W. Wagner, *Ann. Phys.* **40**, 817–855 (1913)
73. R. Jemaï, R. Lahouli, S. Hcini, H. Rahmouni, K. Khirouni, *J. Alloys Compd.* **705**, 340–348 (2017)
74. M. Atif, M. Nadeem, R. Grössinger, R. Sato Turtelli, *J. Alloys Compd.* **509**, 5720–5724 (2011)
75. A.T. Raghavender, K.M. Jadhav, *J. Bull. Mater. Sci.* **32**, 575–578 (2009)
76. D.K. Sandi, A. Supriyanto, A. Jamaluddin, Y. Iriani, *J. Mater. Sci. Eng.* **107**, 012069 (2016)
77. M.A. Ahmed, E. Ateia, L.M. Salah, A.A. El-Gamal, *Phys. Stat. Sol.* **201**, 13 (2004)

78. S.E. Shirsath, R.H. Kadam, A.S. Gaikwad, A. Ghasemi, A. Morisako, J. Magn. Mater. **323**, 3104–3108 (2011)
79. K. Verma, A. Kumar, D. Varshney, J. Alloys Compd. **526**, 91–97 (2012)
80. K. Iwachi, Jpn. J. Appl. Phys. **10**, 1520 (1971)
81. M.A. Iqbal, M. Ul Islam, I. Ali, H.M. Khan, G. Mustafa, I. Ali, J. Ceram. Int. **39**, 1539–1545 (2013)
82. N. Singh, A. Agarwal, S. Sanghi, S. Khasa, J. Magn. Mater. **324**, 2506–2511 (2012)
83. M.A. Ali, M.M. Uddin, M.N.I. Khan, F.U.Z. Chowdhury, S.M. Haque, J. Magn. Mater. **424**, 148–154 (2017)
84. C.B. Mohamed, K. Karoui, S. Saidi, K. Guidara, A.B. Rhaïem, J. Phys. B : Condens. Matter **451**, 87–95 (2014)
85. S.F. Mansour, M.A. Abdo, J. Magn. Mater. **428**, 300–305 (2017)
86. N.H. Vasoya, P.K. Jha, K.G. Saija, S.N. Dolia, K.B. Zankat, K.B. Modi, J. Electron. Mater. **45**, 917 (2016)
87. S. Saha, T.P. Sinha, J. Phys. Rev. B. **65**, 1341 (2005)
88. K.P. Padmasree, D.K. Kanchan, A.R. Kulkarni, J. Solid State Ion. **177**, 475 (2006)
89. M.J. Miah, A.K. Hossain, J. Acta Métal. Sin. **29**, 505–517 (2016)
90. A. Omri, E. Dhahri, M. Es-Souni, M.A. Valente, L.C. Costa, J. Alloys Compd. **536**, 173 (2012)
91. R. Bergman, J. Appl. Phys. **88**, 1356 (2000)
92. K.S. Rao, P.M. Krishna, D.M. Prasad, D. Gangadharudu, J. Mater. Sci. **42**, 4801 (2007)
93. N. Sivakumar, A. Narayanasamy, N. Ponpandian, G. Govindaraj, J. Appl. Phys. **101**, 84116 (2007)
94. R.S. Yadav, I. Kuřitka, J. Vilcakova, J. Havlica, L. Kalina, P. Urbánek, M. Machovsky, D. Skoda, M. Masař, J. Mater. Sci.: Mater. Electron. **29**, 15878–15893 (2018)
95. S. Hcini, A. Omri, M. Boudard, M.L. Bouazizi, A. Dhahri, K. Touileb, J. Mater. Sci.: Mater. Electron. **29**, 6879 (2018)
96. G. Williams, D.C. Watts, Trans. Faraday Soc. **67**, 1971 (1970)
97. M.A. Rahman, A.K.M.A. Hossain, Phys. Scr. **89**, 25803 (2014)
98. S. Khadhraoui, A. Triki, S. Hcini, S. Zemni, M. Oumezzine, J. Magn. Mater. **371**, 69–76 (2014)
99. H. Felhi, R. Lahouli, M. Smari, H. Rahmouni, K. Khirouni, E. Dhahri, J. Mol. Struct. **1179**, 1 (2019)
100. R. Ranjan, N. Kumar, B. Behera, R.N.P. Choudhary, Adv. Mater. Lett. **5138**, 142 (2014)
101. A. Bougoffa, J. Massoudi, M. Smari, E. Dhahri, K. Khirouni, L. Bessais, J. Mater. Sci.: Mater. Electron. **30**, 21018–21031 (2019)
102. W. Hizi, H. Rahmouni, N.E. Gorji, A. Guesmi, N.B. Hamadi, L. Khezami, E. Dhahri, K. Khirouni, M. Gassoumi, J. Catal. **12**, 340 (2022)
103. M. Younas, M. Nadeem, M. Atif, R. Grossinger, J. Appl. Phys. **109**, 93704 (2011)
104. H. Issaoui, A. Benali, M. Bejar, E. Dhahri, B.F.O. Costa, M.P.F. Graca, M.A. Valente, RSC Adv. **10**, 16132–16146 (2020)
105. A. Oueslati, I. Chaabene, K. Adil, F. Hlel, J. Chem. **2013**, 10 (2013)
106. S. Khadhraouia, A. Triki, S. Hcini, S. Zemni, M. Oumezzine, J. Alloys Compd. **574**, 290–298 (2013)

Publisher's Note Springer Nature remains neutral with regard to jurisdictional claims in published maps and institutional affiliations.

Springer Nature or its licensor (e.g. a society or other partner) holds exclusive rights to this article under a publishing agreement with the author(s) or other rightsholder(s); author self-archiving of the accepted manuscript version of this article is solely governed by the terms of such publishing agreement and applicable law.